Differentiation-dependent changes in lamin B1 dynamics and lamin B receptor localization

Chase C. Wesley and Daniel L. Levy*
Department of Molecular Biology, University of Wyoming, Laramie, WY 82071

ABSTRACT **The nuclear lamina serves important roles in chromatin organization and structural support, and lamina mutations can result in laminopathies. Less is known about how nuclear lamina structure changes during cellular differentiation—changes that may influence gene regulation. We examined the structure and dynamics of the nuclear lamina in human-induced pluripotent stem cells (iPSCs) and differentiated germ layer cells, focusing on lamin B1. We report that lamin B1 dynamics generally increase as iPSCs differentiate, especially in mesoderm and ectoderm, and that lamin B receptor (LBR) partially redistributes from the nucleus to cytoplasm in mesoderm. Knocking down LBR in iPSCs led to an increase in lamin B1 dynamics, a change that was not observed for ELYS, emerin, or lamin B2 knockdown. LBR knockdown also affected expression of differentiation markers. These data suggest that differentiation-dependent tethering of lamin B1 either directly by LBR or indirectly via LBR-chromatin associations impacts gene expression.**

Monitoring Editor
Karsten Weis
ETH Zurich

Received: Apr 21, 2022
Revised: Dec 19, 2022
Accepted: Dec 23, 2022

INTRODUCTION

Differentiation is the process by which pluripotent cells divide and change to form the diverse set of specialized tissues necessary for multicellular life. This process occurs within cells of identical genomes, necessitating changes in gene expression. In addition to the roles played by specific transcription factors and growth factors in differentiation, changes in genome organization are also important (Conlon *et al.*, 1994; Mishina *et al.*, 1995; Winnier *et al.*, 1995; Nichols *et al.*, 1998; Beppu *et al.*, 2000; Davis *et al.*, 2004; Peric-Hupkes *et al.*, 2010). A key regulator of genome organization is the nuclear lamina, a meshwork of intermediate filament proteins known as nuclear lamins and lamin-associated proteins that lies beneath the nuclear envelope (Belmont *et al.*, 1993; Guelen *et al.*, 2008; Reddy *et al.*, 2008). The nuclear lamina interacts with lamina-associated domains in the chromatin, typically silencing gene expression at the nuclear periphery (Guelen *et al.*, 2008; Reddy *et al.*, 2008; Meuleman *et al.*, 2013). In this study we begin to address how the structure of the nuclear lamina is regulated during differentiation.

The importance of the nuclear lamina in differentiation and development is underscored by the existence of genetic diseases caused by mutations in nuclear lamina proteins, broadly referred to as laminopathies (Worman and Bonne, 2007; Dobrzynska *et al.*, 2016). The three major lamin genes in mammals are *LMNB1*, *LMNB2*, and *LMNA* (Berezney and Coffey, 1974; Dwyer and Blobel, 1976; Peter *et al.*, 1989; Vorburger *et al.*, 1989; Lin and Worman, 1993). Because the B-type lamins are required for normal development and lamin A expression is extremely low or nondetectable in stem cells, we focus on lamin B1 in the current study, analyzing changes in lamina dynamics during the differentiation of stem cells into the three germ layers. C-terminal deletion of *LMNB1* causes death in mice shortly after birth (Vergnes *et al.*, 2004), while lamin B1 duplications and mutations are known to cause nuclear morphology defects (Padiath *et al.*, 2006; De Castro *et al.*, 2012). Furthermore, lamin B1 mutations are linked to leukodystrophy and microcephaly, while mutations in the major lamina-interacting protein lamin B receptor (LBR) cause Pelger–Huët anomaly and Greenberg skeletal dysplasia (Hoffmann *et al.*, 2002; Waterham *et al.*, 2003; Cristofoli *et al.*, 2020; Parry *et al.*, 2021). LBR is an integral membrane protein consisting of eight transmembrane domains and localized to the inner nuclear membrane. The C-terminal nucleoplasmic domain is

This article was published online ahead of print in MBoC in Press (http://www.molbiolcell.org/cgi/doi/10.1091/mbc.E22-04-0137) on January 4, 2023.

The authors declare no competing interests.

Author contributions: C.C.W. and D.L.L. conceptualized the study; C.C.W. investigated; C.C.W. wrote the original draft; C.C.W. and D.L.L. wrote, reviewed, and edited the article; D.L.L. aquired funding; D.L.L. supervised the study.

*Address correspondence to: Daniel L. Levy (dlevy1@uwyo.edu).

Abbreviations used: eGFP, enhanced green fluorescent protein; FRAP, fluorescence recovery after photobleaching; iPSC, induced pluripotent stem cell; LBR, lamin B receptor; MF, mobile fraction; NE, nuclear envelope; NPC, nuclear pore complex.

relatively short while the N-terminal nucleoplasmic domain binds to chromatin and B-type lamins (Olins *et al.*, 2010; Nikolakaki *et al.*, 2017).

Different methods can be employed to investigate developmental changes in nuclear lamina organization. For example, Dam-ID measures lamina-DNA interactions and BioID generates the nuclear lamina interactome (van Steensel and Henikoff, 2000; Vogel *et al.*, 2007; Guelen *et al.*, 2008; Roux *et al.*, 2012). While these techniques provide large amounts of data with high resolution, they do not inform the dynamics of the nuclear lamina in single cells and often require exogenous perturbation of lamin protein levels. In our study we make use of a genome-edited mEGFP-LMNB1 induced pluripotent stem cell (iPSC) line to minimally disrupt normal lamina function and fluorescence recovery after photobleaching (FRAP) to quantify differentiation-dependent changes in lamin B1 dynamics at the nuclear lamina in intact cells. We find that lamin B1 dynamics at the nuclear envelope (NE) change significantly during differentiation, potentially driven by changes in LBR localization.

RESULTS

Lamin B1 localization and dynamics change upon differentiation

Given that the composition of the nuclear lamina and interactions between lamin proteins and DNA can change during cellular differentiation (Peric-Hupkes *et al.*, 2010), we decided to take an in-depth look at lamin B1 localization and dynamics. We began by immunostaining lamin B1 in an untagged iPSC line and differentiated germ layer cells (endoderm, mesoderm, and ectoderm) derived from those stem cells (Figure 1A). 3D imaging revealed that nuclei in all three types of germ layer cells were flatter compared with iPSCs (Supplemental Figure S1, A and B). To minimize the influence of nuclear height on our lamin B1 measurements, we quantified lamin B1 signal at the NE surface by focusing on the region of the nucleus closest to the coverslip, while nucleoplasmic lamin B1 signal was measured at the central z-slice between the top and bottom lamina surfaces. While most lamin B1 was present at the NE, we also detected a nucleoplasmic population that has been observed in other cell types (Moir *et al.*, 2000; Shimi *et al.*, 2008; Pascual-Reguant *et al.*, 2018). Lamin B1 at the NE and in the nucleoplasm was reduced in all three differentiated cell types compared with iPSCs (Figure 1, B and C). There was no strong correlation between nuclear height and lamin B1 staining intensity except for ectoderm, indicating that our lamin B1 quantification method was largely insensitive to nuclear height (Supplemental Figure S1, C and D).

We next wanted to examine whether lamin B1 dynamics at the nuclear lamina change during differentiation. For this purpose, we performed FRAP at the NE using an eGFP-LMNB1 genome-edited iPSC line. This cell line expresses one copy of lamin B1 tagged at its N-terminus with GFP and was extensively validated by the Allen Institute (Roberts *et al.*, 2017). Although GFP-lamin B1 protein levels are less than untagged lamin B1, total lamin B1 levels are only 9% lower in the eGFP-LMNB1 cell line compared with the parent cell line (Roberts *et al.*, 2017), and the distribution of lamin B1 between the NE and nucleoplasm is similar in both cell lines, with the largest difference of 9% noted in endoderm (Supplemental Figure S1G). Based on superresolution imaging, we find that GFP-tagged lamin B1 and untagged lamin B1 assemble into similar structures within the nuclear lamina, with lamin B1 branch lengths differing by no more than 14% between the two cell lines (Supplemental Figure S1, E and F). GFP tagging of lamin B1 is stable, does not affect cell cycle distribution or cell doubling time, and does not lead to altered karyotype (Roberts *et al.*, 2017). The genome-edited iPSCs exhibit normal morphology, expression of pluripotency markers, and differentiation potential (Roberts *et al.*, 2017). As further evidence that tagged lamin B1 is functional, iPSCs with biallelic N-terminal tagging of lamin B1 are viable and exhibit normal nuclear morphology (Roberts *et al.*, 2017). Given that the lamin B1 C-terminus undergoes extensive processing, N-terminal tagging is typical (Moir *et al.*, 2000; Shimi *et al.*, 2008; Pascual-Reguant *et al.*, 2018), and FRAP on N-terminally tagged lamin B1 has been reported by others (Moir *et al.*, 2000; Dahl *et al.*, 2006; Zhironkina *et al.*, 2016; Pascual-Reguant *et al.*, 2018). Taken together, these data indicate that N-terminal GFP tagging of lamin B1 does not significantly affect nuclear lamina structure, assembly of lamin B1 into the NE, or cell behavior, although undetected effects of the GFP tag remain a formal possibility.

For FRAP experiments, we initially focused on the largest nuclear cross-section and photobleached a region of the nuclear rim. However, this proved to be unreliable because nuclear movements caused the photobleached region to rapidly move out of focus. Instead we focused on the region of the NE closest to the coverslip and photobleached a circular region of eGFP-lamin B1 associated with the NE (Figure 1D), a robust approach used in other studies to quantify lamin dynamics (Kochin *et al.*, 2014; Takeshi *et al.*, 2016; Edens *et al.*, 2017). To ensure we measured lamin B1 dynamics at the NE, the photobleached region was kept in focus during time-lapse imaging by using autofocus along with manual adjustments as needed, and background fluorescence and total nuclear fluorescence were used to normalize for drift (see *Materials and Methods*). Our first observation was that lamin B1 exhibits relatively slow recovery (Figure 1, E and F), perhaps not surprising given that lamin B1 directly associates with the inner nuclear membrane and forms interwoven filaments with the nuclear lamina (Gerace and Blobel, 1980; Turgay *et al.*, 2017). Because there is much less lamin B1 in the nucleoplasm compared with the NE and because nucleoplasmic lamin B1 exhibits very rapid dynamics (Pascual-Reguant *et al.*, 2018), it is unlikely that the slow recovery we observe when photobleaching NE-associated lamin B1 corresponds to nucleoplasmic lamin B1. When photobleaching NE-associated lamin B1, fluorescence recoveries did not generally plateau after 60 min (Figure 1F), or even after 120 min if we extended the imaging time (Supplemental Figure S2A), consistent with previous reports (Moir *et al.*, 2000; Zhironkina *et al.*, 2016). Because performing longer FRAP time lapses to reach steady state was impractical due to the movement of nuclei, we opted to quantify lamin B1 dynamics using somewhat unconventional parameters because fluorescence recoveries were incomplete. Namely, instead of measuring overall mobile fraction, we measured the amount of fluorescence recovery within 60 min of photobleaching. This allowed for differences in recovery to be detected within the given time frame while accounting for differences in initial photobleaching. We refer to this modified mobile fraction measurement as $MF_{0–60\ min}$.

When $MF_{0–60\ min}$ was measured from average normalized recovery curves generated from data for multiple cells, the lamin B1 mobile fraction increased in all three differentiated cell types compared with stem cells, but most significantly in mesoderm (Figure 1G). However, averaging intensity values at each time point for multiple nuclei obscures statistically significant differences due to cell-to-cell variability. If instead we measured $MF_{0–60\ min}$ for individual nuclei and then averaged those values for a given cell type, all three differentiated cell types exhibited significant increases in mobile fraction relative to stem cells, ranging from 57 to 75% (Figure 1H). Ultimately, we decided the latter method more accurately reflects

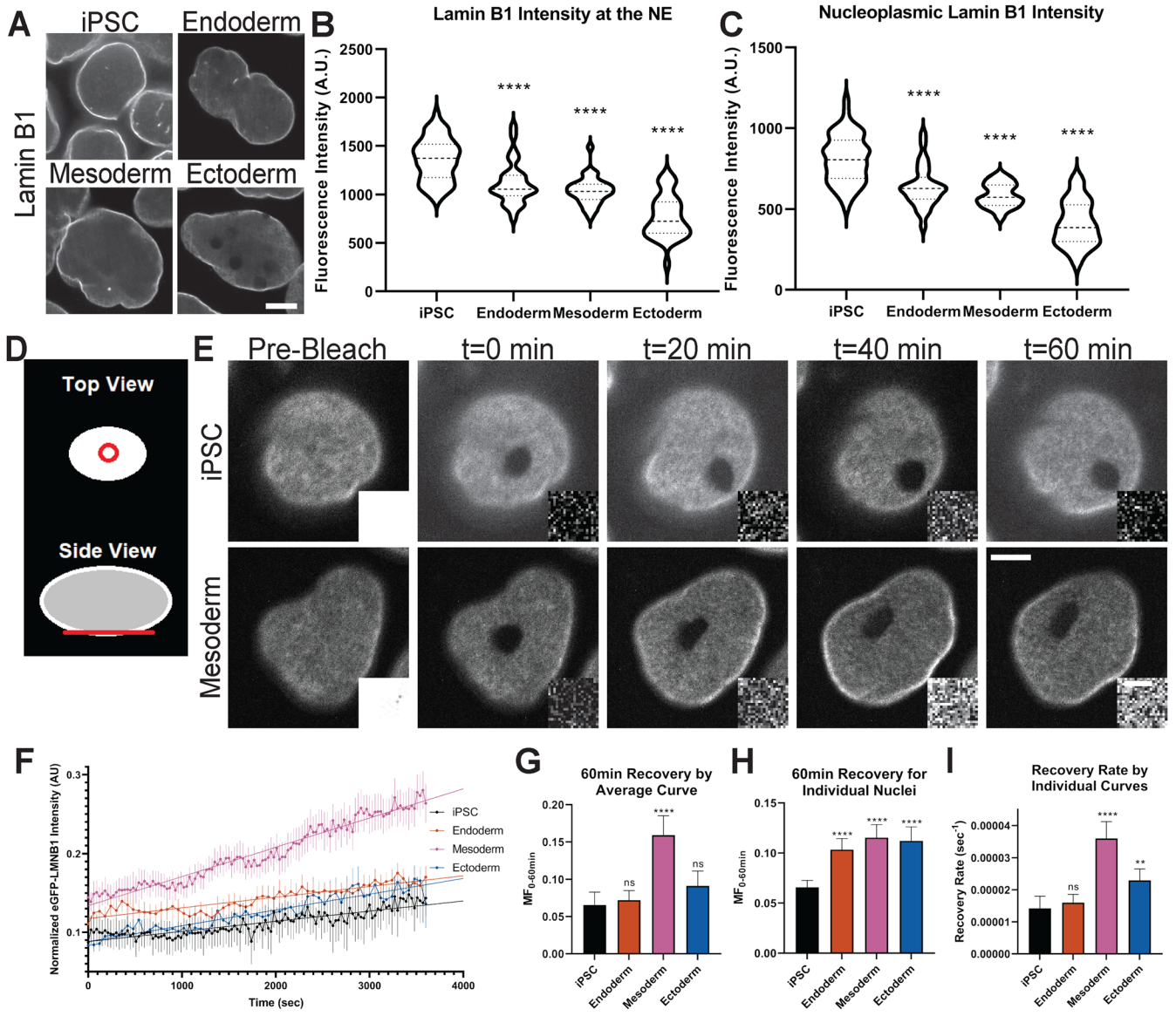

FIGURE 1: Lamin B1 localization and dynamics change during differentiation. (A–C) An untagged iPSC line was differentiated into germ layer cells and immunostained for lamin B1. (A) Representative images are shown. Scale bar: 5 μm. (B) Focusing on the region of the NE closest to the coverslip, lamin B1 intensity at the nuclear lamina was measured for 52 iPSCs, 29 endoderm cells, 34 mesoderm cells, and 34 ectoderm cells. (C) Focusing on the largest nuclear cross-section, lamin B1 intensity in the nucleoplasm was measured for the same cells as in B. (D–I) Genome-edited eGFP-LMNB1 cells were photobleached at the nuclear lamina and FRAP time lapses were acquired (60 min for iPSC and mesoderm, 120 min for endoderm and ectoderm, 2 prebleach images, 121 postbleach images at regular intervals). (D) Diagram showing how a circular region of eGFP-lamin B1 within the NE closest to the coverslip was photobleached (red lines). (E) Images from representative time lapses are shown. Larger boxes represent whole nuclei. Smaller boxes represent the photobleached region with brightness and contrast identically adjusted for a given cell type to more clearly visualize recovery. Scale bars: 5 μm for larger box, 1 μm for smaller box. (F) Average fluorescence recovery curves based on normalized data (see *Materials and Methods*) and linear regressions are shown. Data were acquired for 91 iPSC nuclei, 55 endoderm nuclei, 59 mesoderm nuclei, and 57 ectoderm nuclei. (G) $MF_{0–60\ min}$ was calculated from the average curves shown in F, as described in *Materials and Methods*. (H) $MF_{0–60\ min}$ values were calculated for individual nuclei and averaged as described in *Materials and Methods*. Data were acquired for 88 iPSC nuclei, 54 endoderm nuclei, 57 mesoderm nuclei, and 56 ectoderm nuclei. (I) Recovery rates were calculated for individual nuclei and averaged as described in *Materials and Methods*. Data were acquired for 88 iPSC nuclei, 51 endoderm nuclei, 58 mesoderm nuclei, and 57 ectoderm nuclei. $MF_{0–60\ min}$, mobile fraction over 60-min interval. Cumulative data from four, six, seven, and four independent trials are presented for iPSCs, endoderm, mesoderm, and ectoderm, respectively. All error bars are 95% confidence intervals. On violin plots, solid line represents median and dashed line represents quartiles. One-way ANOVA with Dunnett's multiple comparisons statistical tests were performed, with significance relative to iPSC shown. ns, not significant; **, $p < 0.01$; ****, $p < 0.0001$.

the raw data and so average $MF_{0–60\ min}$ values from individual nuclei are reported throughout the rest of this study. We also measured the linear recovery rate based on a linear fit, which generates different information from $MF_{0–60\ min}$ that is determined by the maximum change in intensity of the raw unfitted data. Similar to mobile fraction measurements, lamin B1 recovery rates increased in all differentiated cell types relative to stem cells, but most significantly in mesoderm and ectoderm where lamin B1 recovery rates increased 152 and 61%, respectively (Figure 1I). These data show that lamin B1 becomes generally more dynamic as stem cells differentiate into cells of the three germ layers.

Cell cycle state is not primarily responsible for changes in lamin B1 dynamics during differentiation

One factor that could potentially influence lamin B1 dynamics is cell cycle state. We first examined whether the cell cycle distribution differs in the cell types under analysis by staining cells with Hoechst after FRAP analysis and estimating the cell cycle state from total fluorescence intensity (Roukos *et al.*, 2015). While 62% of iPSCs were in G1, we observed an increase in S-phase cells in mesoderm and G2-phase cells in ectoderm (Supplemental Figure S4, A and B). To determine whether these changes in cell cycle distributions could account for observed differences in lamin B1 dynamics, we quantified $MF_{0–60\ min}$ and recovery rates as a function of cell cycle state. Cell cycle state had no significant effect on lamin B1 dynamics in iPSCs and ectoderm (Supplemental Figure S4, C–E). We did note a slight reduction in lamin B1 $MF_{0–60\ min}$ in mesoderm S- and G2-phase cells compared with G1-phase cells (Supplemental Figure S4D). However, this cannot account for the overall increased lamin B1 dynamics observed in mesoderm compared with iPSCs (Figure 1, F–I). Taken together, these data suggest that cell cycle state is not responsible for observed cell type–dependent changes in lamin B1 dynamics.

LBR localization changes during differentiation

Having observed differentiation-dependent changes in lamin B1 dynamics, we next turned our attention to determining what factors might be regulating these changes. We focused on the levels and localizations of four NE proteins: LBR, emerin, ELYS, and lamin B2. We chose LBR for its established role in binding lamin B1 and chromatin as well as its role in differentiation (Olins *et al.*, 2010). We selected emerin as a representative example of a LEM domain protein and ELYS for its role in linking the lamina to nuclear pore complexes (NPCs; Berk *et al.*, 2013; Kittisopikul *et al.*, 2021; Wong *et al.*, 2021). We chose lamin B2 because it represents another ubiquitous lamina protein (Broers *et al.*, 1997). Immunoblots showed that there were no large (greater than threefold) differentiation-dependent changes in the levels of any of these proteins, although emerin expression did decrease with differentiation while ELYS expression increased in endoderm and ectoderm cells (Figure 2, A and B).

We next used immunofluorescence to determine whether the distribution of any of these four NE proteins changes during differentiation (Figure 2C). Although subtle differences were observed for all four proteins (Supplemental Figure S3), LBR distribution changed the most significantly. While predominantly nuclear in stem cells, LBR exhibits cytoplasmic puncta in endoderm and, more significantly, in mesoderm (Figure 2, C and D). Given that LBR is known to translocate from the ER to nucleus, these cytoplasmic puncta likely represent ER-localized LBR (Ellenberg *et al.*, 1997; Zuleger *et al.*, 2011). If LBR is an important anchor that restricts lamin B1 movement, observing relatively less nuclear LBR in mesoderm cells could explain why lamin B1 is more dynamic in mesoderm cells compared with stem cells (Figure 1, D–I). These data indicate significant reorganization of some nuclear lamina components during early differentiation.

Although some previous studies reported low or undetectable levels of lamin A/C in stem cells (Rober *et al.*, 1989; Constantinescu *et al.*, 2006; Zuo *et al.*, 2012), we observed lamin A/C in iPSC nuclei that was increased in endoderm but reduced in mesoderm and ectoderm (Supplemental Figure S5, A and B). NPC densities were not significantly different between iPSCs and differentiated cells (Supplemental Figure S5, C and D). We also examined the distribution of heterochromatin by H3K9me3 staining, finding a 30% reduction in the amount of heterochromatin localized close to the nuclear lamina in mesoderm compared with iPSCs but no significant changes in endoderm or ectoderm (Supplemental Figure S5, E and F). Reduced heterochromatin at the NE in mesoderm cells might contribute to increased lamin B1 dynamics or vice versa. These data indicate that lamin A/C levels, NPC densities, and heterochromatin distribution do not generally correlate with differentiation-dependent changes in lamin B1 dynamics.

LBR modulates lamin B1 dynamics

To determine whether emerin, ELYS, lamin B2, and most notably LBR affect Lamin B1 dynamics, we repeated our FRAP experiments after individual RNAi knockdown of these genes (Figures 3 and 4, and Supplemental Figures S2 and S4, F–J). We also included an LBR/ELYS double knockdown, given the known role ELYS plays in the localization of LBR (Clever *et al.*, 2012); although this treatment could impact cell cycle progression, we did not observe any effects on cell numbers or obvious mitotic defects. To focus and simplify our efforts, the two differentiated cell lines with the greatest changes in dynamics, mesoderm and ectoderm, were studied along with iPSCs. LBR and LBR/ELYS knockdowns in iPSCs led to similar increases in the lamin B1 $MF_{0–60\ min}$ (Figure 3, A and B), so we attribute this effect to LBR knockdown. Notably, the mobile fraction increase of 43% upon knocking down LBR in iPSCs (Figure 3B) approaches the 75% increase observed when iPSCs differentiate into mesoderm (Figure 1H), suggesting LBR may be a key determinant of differences in lamin B1 dynamics between iPSCs and mesoderm.

We also performed FRAP experiments in mesoderm cells after RNAi knockdown (Figure 4A). None of the knockdowns induced a significant change in $MF_{0–60\ min}$, although the lamin B1 recovery rate was somewhat reduced upon LBR/ELYS double knockdown (Figure 4, B and C). For completeness, we performed similar experiments in ectoderm cells, where LBR, ELYS, lamin B2, and LBR/ELYS knockdowns reduced the lamin B1 recovery rate (Supplemental Figure S2, B–D). These knockdown results in mesoderm and ectoderm suggest the LBR tethering effect on lamin B1 dynamics is less evident in differentiated cell types and highlight the specificity of LBR to restrict lamin B1 dynamics in iPSCs. Further studies will be necessary to understand how these different NE proteins regulate lamin B1 dynamics in differentiated cell types.

LBR influences differentiation marker expression

Given the role LBR plays in regulating lamin B1 dynamics during differentiation, we decided to examine whether LBR influences expression of pluripotency markers Oct4 and Nanog and differentiation markers HNF-3β, Brachyury, and Otx2 in iPSCs by knocking down LBR and performing immunofluorescence (Figure 5; Ang *et al.*, 1993; Jacob *et al.*, 1997; Smith, 1997; Nichols *et al.*, 1998; Beby and Lamonerie, 2013; Saunders *et al.*, 2013). LBR knockdown resulted in a 13% decrease in Oct4 expression and a 70% increase in HNF-3β expression, suggesting a shift away from pluripotency

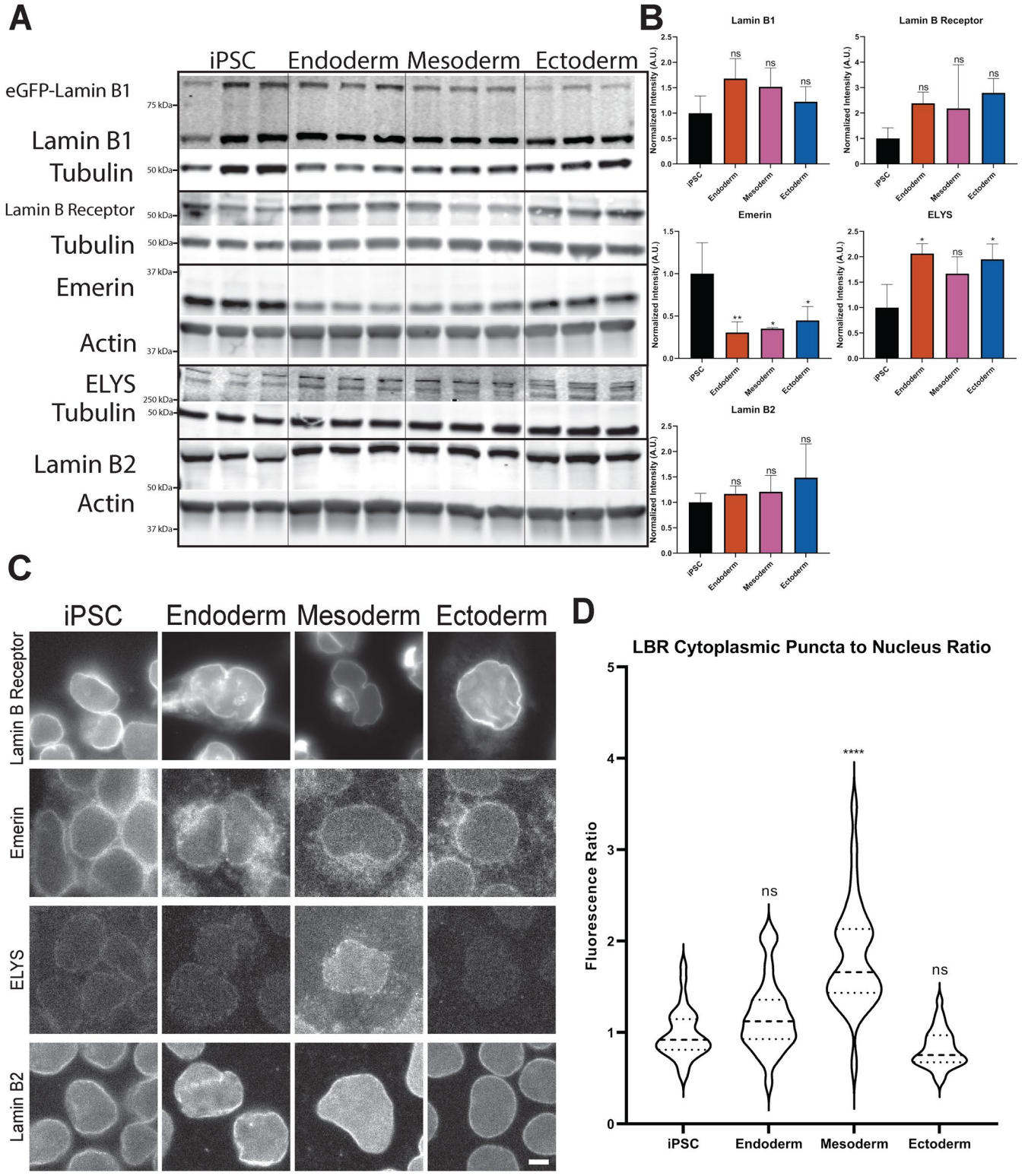

FIGURE 2: Changes in nuclear envelope protein levels and localization during differentiation. (A) Immunoblots were performed on whole cell lysates for the indicated proteins. Three independent samples for each cell type were analyzed. (B) Quantification of protein levels from immunoblots shown in A, normalized to Ponceau staining intensity. Endogeneous and eGFP-lamin B1 bands were combined to report on total lamin B1 levels. (C) Representative immunofluorescence images. Weak emerin and ELYS signals likely reflect their relatively low expression levels in these cell types. Scale bar: 5 μm. (D) Ratio of LBR in cytoplasmic puncta vs. the nucleus for 30 nuclei per cell type. All error bars are 95% confidence intervals. On violin plots, solid line represents median and dashed line represents quartiles. One-way ANOVA with Dunnett's multiple comparisons statistical tests were performed, with significance relative to iPSC shown. ns, not significant; *, $p < 0.05$; **, $p < 0.01$; ****, $p < 0.0001$.

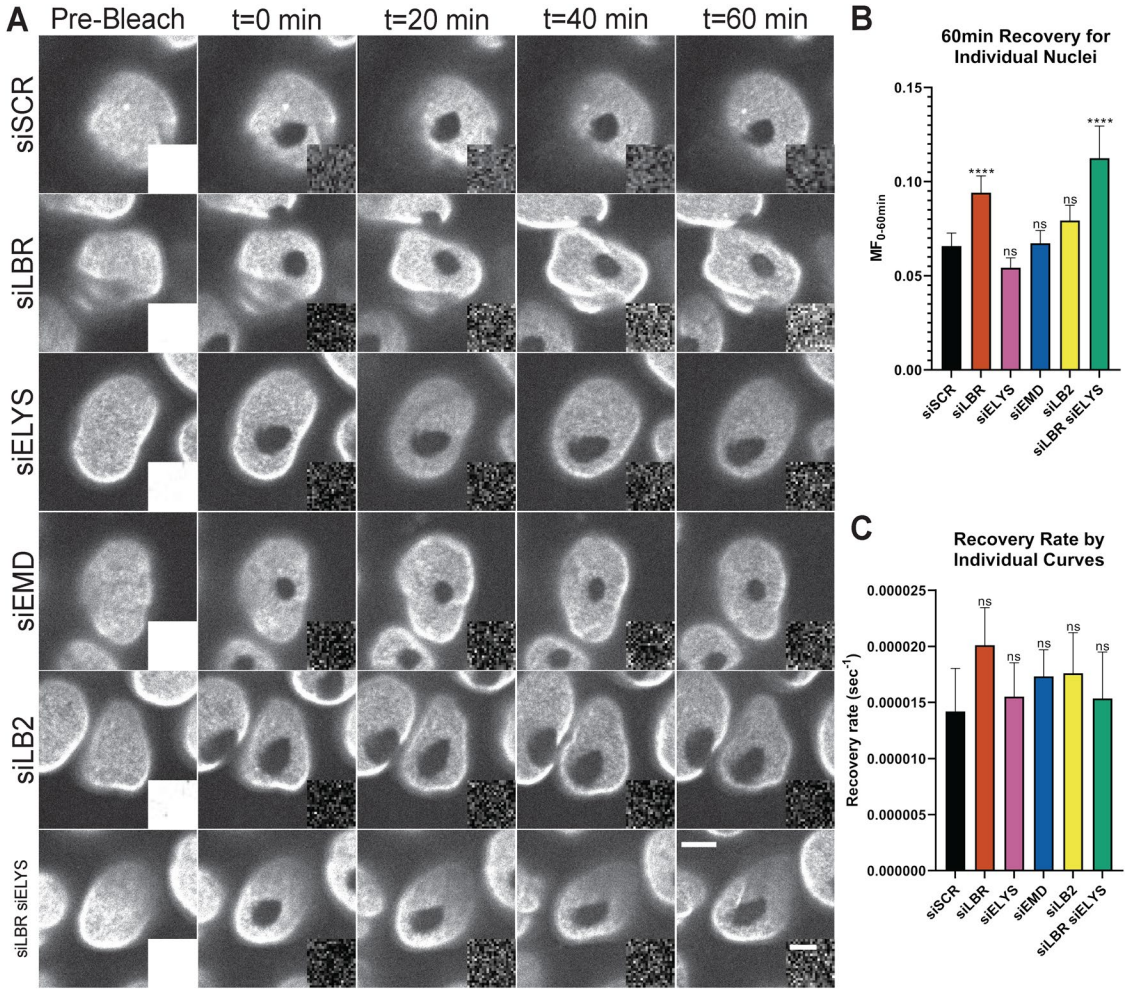

FIGURE 3: Lamin B1 dynamics in knockdown iPSCs. eGFP-LMNB1 iPSCs were transfected with siRNAs targeting negative control (siSCR; same iPSC data presented in Figure 1), LBR (siLBR), ELYS (siELYS), emerin (siEMD), lamin B2 (siLB2), or both LBR and ELYS (siLBR siELYS). FRAP experiments were performed and analyzed as in Figure 1. (A) Images from representative time lapses are shown. Larger boxes represent whole nuclei. Smaller boxes represent the photobleached region with brightness and contrast identically adjusted for a given knockdown to more clearly visualize recovery. Scale bar: 5 μm for larger box, 1 μm for smaller box. (B) $MF_{0–60\ min}$ values were calculated for individual nuclei and averaged. Data were collected for 88 siSCR nuclei, 73 siLBR nuclei, 91 siELYS nuclei, 102 siEMD nuclei, 89 siLB2 nuclei, and 61 siLBR siELYS nuclei. (C) Recovery rates were calculated for individual nuclei and averaged for 88 siSCR nuclei, 77 siLBR nuclei, 91 siELYS nuclei, 96 siEMD nuclei, 87 siLB2 nuclei, and 49 siLBR siELYS nuclei. Cumulative data from four, three, four, four, three, and five independent trials are presented for siSCR, siLBR, siELYS, siEMD, siLB2, and siLBR siELYS, respectively. All error bars are 95% confidence intervals. One-way ANOVA with Dunnett's multiple comparisons statistical tests were performed, with significance relative to siSCR shown. ns, not significant; ****, $p < 0.0001$.

and toward differentiation (Figure 5B). However, the expression pattern was complicated, as Nanog expression increased and Brachyury expression decreased (Figure 5B). So, while it is clear that LBR influences expression of some differentiation markers, there is not a clear link to stemness versus differentiated. Nonetheless, these data suggest a role for LBR in the regulation of cellular differentiation.

DISCUSSION

Overall, we show that lamin B1 dynamics increase during iPSC differentiation into germ layer cells. The larger nonexchangeable fraction of lamin B1 in iPSCs may help to maintain a stable gene expression state characteristic of pluripotency, while a more dynamic lamina in differentiating cells may help to actively modify gene expression patterns. This differentiation-dependent change in lamin B1 dynamics does not correlate with cell cycle state but instead relates to changes in the protein composition of the nuclear lamina. We propose that LBR acts as a lamin B1 tether in iPSCs that is partially released in mesoderm cells in a differentiation-dependent manner. However, because LBR is a relatively mobile protein (Ellenberg *et al.*, 1997; Zuleger *et al.*, 2011), it could be that LBR does not directly influence lamin B1 dynamics. Given that LBR associates with heterochromatin at the nuclear periphery (Solovei *et al.*, 2013; Lukasova *et al.*, 2017) and that we observed reduced heterochromatin at the NE in mesoderm compared with iPSCs, another model is that LBR directly impacts the association of chromatin with the NE and that this in turn affects lamin B1 dynamics. Thus, changes in lamin B1 dynamics during differentiation might be regulated by LBR localization and/or chromatin organization.

All of our measurements of lamin B1 dynamics rely on photobleaching of GFP-tagged lamin B1. Although our analysis of this

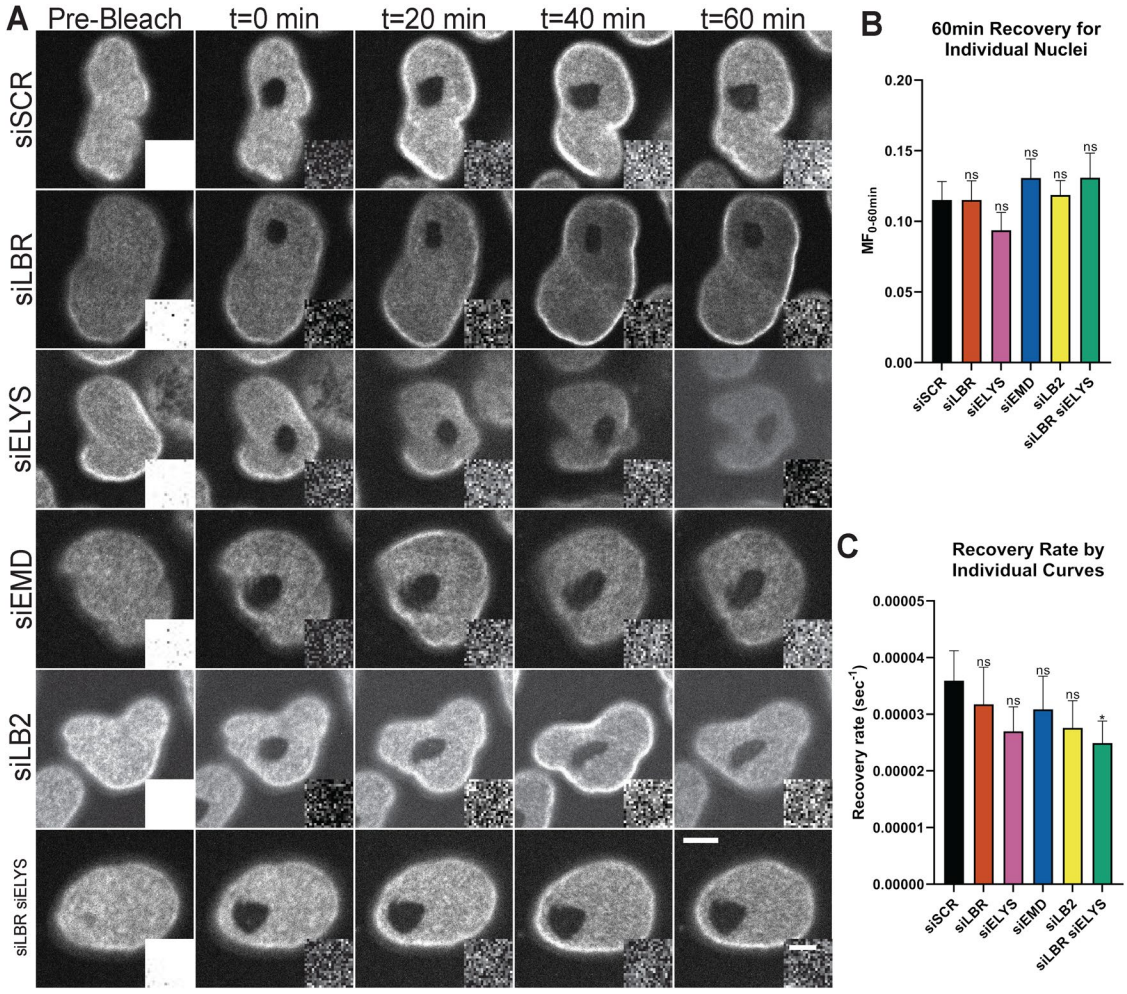

FIGURE 4: Lamin B1 dynamics in knockdown mesoderm cells. Experiments were performed as in Figure 3 with mesoderm cells (siSCR; same mesoderm data presented in Figure 1). (A) Images from representative time lapses are shown. Larger boxes represent whole nuclei. Smaller boxes represent the photobleached region with brightness and contrast identically adjusted for a given knockdown to more clearly visualize recovery. Scale bar: 5 μm for larger box, 1 μm for smaller box. (B) $MF_{0–60\ min}$ values were calculated for individual nuclei and averaged. Data were collected for 57 siSCR nuclei, 62 siLBR nuclei, 60 siELYS nuclei, 63 siEMD nuclei, 76 siLB2 nuclei, and 62 siLBR siELYS nuclei. (C) Recovery rates were calculated for individual nuclei and averaged. Data were collected for 58 siSCR nuclei, 62 siLBR nuclei, 59 siELYS nuclei, 59 siEMD nuclei, 75 siLB2 nuclei, and 60 siLBR siELYS nuclei. Cumulative data from seven, three, two, four, four, and five independent trials are presented for siSCR, siLBR, siELYS, siEMD, siLB2, and siLBR siELYS, respectively. All error bars are 95% confidence intervals. One-way ANOVA with Dunnett's multiple comparisons statistical tests were performed, with significance relative to siSCR shown. ns, not significant; *, $p < 0.05$.

CRISPR-modified cell line suggests that the N-terminal fusion does not significantly affect nuclear lamina structure, assembly of lamin B1 into the NE, or cell behavior, caveats remain with regard to interpretation of these experiments. The GFP tag could alter the dynamic properties or behavior of lamin B1 compared with the endogenous protein. If this is the case, then the absolute measurements of mobile fractions and recovery rates that we report here may not accurately reflect those parameters for the endogenous untagged lamin B1. Nonetheless, we would expect the relative differences between cell types and upon knockdown to still be valid and informative.

While the lamin B1 mobile fraction and recovery rate did increase upon LBR knockdown in iPSCs, the change in recovery rate was not statistically significant (Figure 3). Changes in mobile fraction are perhaps more physiologically relevant in terms of how chromatin-lamina interactions affect gene expression (Peric-Hupkes *et al.*, 2010). For example, it is possible that the nonexchangeable fraction of lamins, which is related to the mobile fraction, has a greater effect on chromatin association and gene expression than how quickly the lamins associate and dissociate, meaning the recovery rate of the exchangeable fraction may be less physiologically relevant. Furthermore, given that cells spend hours in interphase, a change in the recovery rate of a few seconds or minutes is likely insignificant compared with a change in the mobile fraction. Regardless, LBR can act as a tether for lamin B1, a function that may have relevance in differentiation.

Knockdown of LBR, ELYS, emerin, or lamin B2 in mesoderm cells minimally affected lamin B1 dynamics (Figure 4). This could be because of LBR's reduced nuclear localization in mesoderm (Figure 2, C and D) or because lamin B1 dynamics have perhaps reached a threshold. It is also possible that the lamin B1 interactome in mesoderm is sufficiently different from that in iPSCs, so the knockdowns

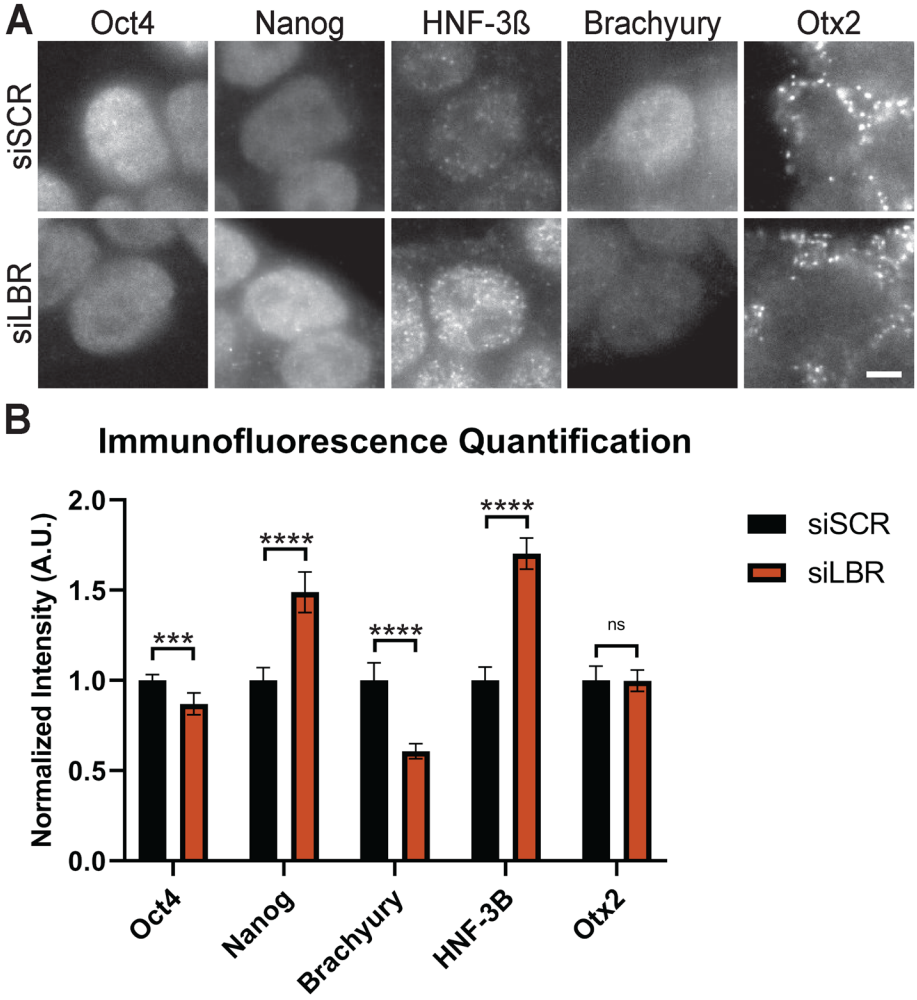

FIGURE 5: LBR knockdown alters the levels of pluripotency and differentiation marker proteins. eGFP-LMNB1 iPSCs were transfected with negative control siRNA (siSCR) or LBR siRNA (siLBR) and imaged by immunofluorescence for pluripotency and differentiation factors. (A) Representative images are shown. Scale bar: 5 µm. (B) Mean nuclear fluorescence intensities were measured for 240 control and 260 LBR knockdown nuclei for Oct4 and 90 nuclei for all other groups. For each antibody staining, normalization was to the siSCR control. All error bars are 95% confidence intervals. Two-tailed, heteroscedastic *t* tests were performed. ns, not significant; ***, $p < 0.001$; ****, $p < 0.0001$.

tested have differential effects on lamin B1 dynamics. Nonetheless, we demonstrate a cell-type-specific role for LBR in regulating lamin B1 dynamics and expression of differentiation markers, thus warranting further research. In particular, interactome studies will provide mechanistic insights into the regulation of lamin B1 dynamics. Extending these studies to other cell types and in the context of laminopathies will inform how lamin B1 and LBR dynamics promote normal development and differentiation while possibly being dysregulated in some disease states.

MATERIALS AND METHODS

Request a protocol through *Bio-protocol*.

Antibodies

The following antibodies were utilized at the indicated concentrations: rabbit anti–lamin B1 used at 0.7 µg/ml for Western blotting and 0.35 µg/ml for immunofluorescence (Abcam; ab16048), rabbit anti-Nanog used at 1:100 for immunofluorescence and 1:1000 for Western blotting (Abcam; ab109250), mouse anti-HNF-3β used at 1:50 for immunofluorescence and 1:200 for Western blotting (Santa Cruz Biotechnology; sc-101060), mouse anti–α-tubulin (DM1A) used at 1:1000 for Western blotting (Santa Cruz Biotechnology; sc-32293), rabbit anti–β-actin used at 1:1000 for Western blotting (RevMAb Biosciences; 31-1013-00), rabbit anti-Oct4 used at 1:1000 for immunofluorescence and 1:5000 for Western blotting (Thermofisher Scientific; PA5-27438), mouse anti–Otx-2 used at 1:50 for immunofluorescence and 1:100 for Western blotting (Santa Cruz Biotechnology; sc-514195), rabbit anti-Brachyury used at 1:200 for immunofluorescence and 1:1000 for Western blotting (Abgent; AP20187a), mouse anti-Oct used at 1:200 for immunofluorescence and 1:500 for Western blotting (Stem Cell Technologies; 50093.1), mouse anti-emerin used at 1:200 for immunofluorescence and 1:100 for Western blotting (Santa Cruz Biotechnology; sc-25284), mouse anti–lamin B2 used at 1:500 for immunofluorescence and 1:500 for Western blotting (GeneTex; GTX628803), mouse anti-ELYS used at 1:50 for immunofluorescence (Santa Cruz Biotechnology; sc-81265), rabbit anti-ELYS used at 1:100 for Western blotting (Bethyl Labs; A300-166A), rabbit anti–LBR used at 1:100 for immunofluorescence and 1:1000 for Western blotting (ABclonal; A5468), mouse anti–lamin A/C used at 1:1000 for immunofluorescence (Santa Cruz Biotechnology; sc-376248), mouse anti–nuclear pore complex used at 1:1000 for immunofluorescence (mAb414; Biolegend; 902901), mouse anti-histone H3K9me3 used at 1:100 for immunofluorescence (Active Motif; 39285), goat anti-rabbit IgG H&L Alexa Fluor 405 used at 1:200 for immunofluorescence (Abcam; ab175652), donkey anti-mouse IgG H+L Alexa Fluor 647 used at 1:1000 for immunofluorescence (ThermoFisher; A-31571), IRDye 680RD goat anti-mouse IgG used at 1:15,000 for Western blotting (Li-Cor; 926-68070), and IRDye 800RD anti-rabbit IgG used at 1:20,000 for Western blotting (Li-Cor; 926-32211).

Immunofluorescence

For immunofluorescence staining, cells were grown on acid-washed 22 mm × 22 mm square no. 1½ glass coverslips (Corning; 2850-22). Cells on coverslips were washed three times in phosphate-buffered saline (PBS) for 5 min per wash, then fixed using 4% paraformaldehyde for 15 min. Cells on coverslips were then washed three times in PBS for 5 min per wash and permeabilized with 0.1% Triton X-100 for 10 min. After three more 5-min PBS washes, cells were blocked in 10% goat serum (Sigma; G9023) and 0.3 M glycine in PBS for 1 h. Three 5-min washes in PBS were repeated and cells were stained overnight in primary antibody solution (2% goat serum in PBS with appropriate primary antibodies). After three more 5-min PBS washes, cells were incubated with secondary antibody solution

(2% goat serum in PBS with appropriate secondary antibodies) for 75 min. Coverslips were then washed three times in PBS for 5 min per wash, briefly washed twice with dH_2O, mounted on microscope slides using VECTASHIELD antifade mounting medium (Vector Laboratories; H-1000), and sealed with nail polish.

Cell culture

All iPSCs were cultured as described previously (Roberts *et al.*, 2017). Untagged iPSCs (Coriell Institute for Medical Research; GM25256) and mEGFP-tagged LMNB1 iPSCs (Allen Institute for Cell Science, Coriell; AICS-0013 cl.210) were grown in mTeSR and mTeSR Plus in cell culture dishes coated with Matrigel matrix (Growth Factor Reduced; Corning; 354230, or phenol-red-free; Corning; 356237). Matrigel was applied at a concentration of 137–154 µg/ml dissolved in PBS or DMEM. Cells were dissociated using Gentle Cell Dissociation Reagent (Stem Cell Technologies; 100-0485) or Versene Solution (Thermofisher Scientific; 15040066) and ROCK Inhibitor Y27632 at a final concentration of 10 µM (ATCC; ACS-3030). iPSCs were differentiated using STEMdiff Trilineage Differentiation Kit (Stem Cell Technologies; 05230) or STEMdiff Mesoderm Induction Medium (Stem Cell Technologies; 05220). All cells were maintained at 37°C at 5% CO_2. Pluripotency and differentiation were confirmed using Oct4, Nanog, HNF-3β, Otx-2, and Brachyury antibodies in immunofluorescence assays.

siRNAs

For RNAi experiments, the following siRNAs were used: ELYS (Ambion; s24727, 4392420), emerin (consisted of the following duplex sequences: "rArCrGrArCrUrArCrUrArUrGrArArGrArGrArGrCrUrArCTT" and "rArArGrUrArGrCrUrCrUrCrUrUrCrArUrArGrUrArGrUrCrGrUrCrA"; Integrated DNA Technologies), LBR (Santa Cruz Biotechnologies; sc-88544), lamin B2 (Ambion; s39477; catalog number 4427037), and negative control (Ambion; 4390843).

Western blots

Whole cell lysates were prepared using RIPA buffer and incubated on ice for 30 min, after which lysates were centrifuged to pellet insoluble cellular debris and snap-frozen in liquid nitrogen. For normalization, lysate protein concentrations were measured using a EZQ Protein Quantitation Kit (Thermofisher; R33200). Lysate proteins were separated on 7% (for ELYS) or 10% SDS–PAGE gels. Proteins were transferred to PVDF by semidry transfer for all blots expect ELYS, which utilized wet transfers. Membranes were then blocked in 5% milk in PBS, probed with primary antibodies overnight, and stained with Li-Cor Odyssey secondary antibodies (see *Antibodies* section). Blots were then scanned using a Li-Cor Odyssey CLx imager. Band intensities were quantified using ImageJ software and normalized for background signal. To quantify total protein, blots were stained with Ponceau (0.1% wt/vol Ponceau in 5% acetic acid), destained in 5% acetic acid, imaged on a BioRad ChemiDoc MP imager, analyzed using ImageJ software, and normalized for background signal (Schindelin *et al.*, 2012).

Microscopy

Fluorescence microscopy images were acquired using an Olympus BX63 upright wide-field epifluorescence microscope equipped with an X-Cite 120 LED illumination system and a Hamamatsu ORCA-Flash4.0 digital CMOS high-resolution camera. The objective used was an Olympus UPlanSApo 40× (NA 1.25; silicon oil). Image acquisition was controlled using a motorized Olympus stage and Olympus CellSens software. Confocal microscopy images were obtained using an Olympus IX81 microscope stand equipped with a Yokogawa CSU-X1 spinning-disk confocal head, a five-line LMM5 laser launch (Spectral Applied Research), and Hamamatsu ORCA-Flash4.0 C114400 digital CMOS camera. Samples were maintained at 37°C and 5% CO_2 with a stage-top incubator (Tokai Hit; INUBG2A-ZILCS). An Olympus UPlanSApo 60×/1.20 water immersion objective was used. For confocal FRAP experiments an iLas2 system was used. Confocal superresolution microscopy images were acquired using an Olympus IX83 inverted confocal microscope equipped with an IXplore SpinSR microscope system, a Coherent OBIS LX 405 nm, 50 mW laser system (SKU 1284370), a Coherent OBIS LS 488 nm, 100-mW laser system (SKU 1226420), a Coherent OBIS LS 561 nm, 100-mW laser system (SKU 1253302), a Coherent OBIS LX 640 nm, 100-mW laser system (SKU1178790), a Yokogawa CSU-W1 SoRa confocal scanner unit, ORCA-Fusion C14440 digital cameras, and an Olympus U-RTCE real-time controller. Image acquisition was controlled using a motorized Olympus stage, a Marzhauser Wetzlar TANGO Desktop controller, and CellSens software. The objective used was an Olympus UPlanSApo 100× (NA 1.35; silicon oil) with a 3.2× magnification changer for superresolution imaging. Nuclei were analyzed as z-stacks with a 0.2-µm step size for most experiments including superresolution imaging for nuclear height, nucleoplasmic and lamina fluorescence intensities, and lamin B1 skeleton analysis. Image acquisition with a 1-µm step size was used for nuclei stained for H3K9me3.

Image analysis

To measure signal intensity in the nucleoplasm and at the NE, 3.25-µm square regions were selected at the center of the nucleus in the middle z-plane and at an even section on the lamina surface closest to the coverslip, respectively, and average fluorescence intensity was measured. A background region was selected for each image and used to apply background subtraction to the measured intensity values. All analyses were conducted with ImageJ software. For NE to nucleoplasm line scan measurements, ImageJ was used to draw a line across each nucleus and the peak fluorescence values were identified and defined as the NE region (Schindelin *et al.*, 2012). The region between these peaks was then defined as the nucleoplasmic region. The maximum intensity value for the NE region was divided by the average intensity of the nucleoplasmic region to determine the NE to nucleoplasm ratio. To calculate the nucleus to cytoplasmic fluorescence ratios, regions were drawn around the nuclear and cytoplasmic regions of each cell of interest using ImageJ, then the average intensity of the nuclear region was divided by the average intensity of the cytoplasmic region (excluding the nuclear region; Schindelin *et al.*, 2012). To calculate the cytoplasmic puncta to nucleus ratio, a line was drawn in ImageJ across the nucleus and the brightest extranuclear puncta in each cell of interest (Schindelin *et al.*, 2012). For each cell, average fluorescence intensity values were calculated for the nucleus and for the cytoplasmic puncta. The resulting average for the cytoplasmic puncta was then divided by the average for the nucleus. To quantify knockdowns by immunofluorescence, cells were analyzed with ImageJ by drawing regions of interest around cells and measuring average fluorescence, then correcting with background subtraction. To quantify expression of stem and differentiation markers by immunofluorescence, cells were analyzed with ImageJ by drawing regions of interest around nuclei and measuring average fluorescence, then correcting with background subtraction.

To measure lamin B1 branch length, nuclei were immunostained for lamin B1 and imaged by superresolution microscopy on the nucleus surface. The auto contrast feature in ImageJ was used to

enhance visualization of lamin B1 branches. A Gaussian blur with a sigma of 0.040625 µm was applied to the images before thresholding to prevent detection of extraneous branches. A 10.563 μm^2 square section was selected at the lamina of each nucleus in ImageJ followed by skeletonization and measurement of branch lengths as described in Fiserova *et al.* (2019). To quantify lamin A/C using ImageJ, nuclei were immunostained for lamin A/C and selected by either thresholding and segmentation using the watershed function or manually if nuclei could not be accurately segmented. Nuclear lamin A/C intensity was then measured after background subtraction. To quantify NPC density, superresolution images of mAb414-stained nuclei were acquired at the NE surface. NPCs within a 5.941-μm^2 square region were counted in ImageJ. To account for differences in image signal intensity, brightness and contrast were adjusted to enhance visualization of NPCs, and NPCs were counted based on the appearance of distinct puncta at the NE. To quantify the fluorescence of H3K9me3 at the nuclear lamina, eGFP-lamin B1 cells were immunostained for H3K9me3 and quantification performed in ImageJ on each background subtracted slice of a z-stack. Nuclei were first thresholded based on the GFP-lamin B1 channel to select the whole nucleus and the H3K9me3 integrated density was measured. Next the H3K9me3 integrated density of the nucleoplasmic region not associated with the nuclear lamina was measured. If thresholding in this way could not distinguish adjacent nuclei, regions of interest were manually selected. Values below background were excluded. The nucleoplasmic signal was subtracted from the whole nucleus signal to give the total background subtracted integrated density of H3K9me3 signal near the nuclear lamina. Average H3K9me3 fluorescence intensity close to the nuclear lamina was calculated by dividing the total integrated density by the area of the lamina proximal region.

FRAP experiments

Cells were cultured in µ-Slide 2 Well dishes (Ibidi; 80286) coated with Matrigel. Photobleaching of eGFP-lamin B1 at the NE was accomplished with five pulses of a 405-nm laser set at 100% power in a circular region 0.9 µm in diameter. Time lapses were acquired with two prebleach time points and 121 postbleach time points. For 1-h time lapses, the interval between time points was 30 s, while the interval was 60 s for 2-h time lapses. FRAP time lapses were analyzed using ImageJ Fiji software recording the mean fluorescence of the bleached region, the whole nucleus, and a background region for each time point (Schindelin *et al.*, 2012). If necessary, we corrected for movement of nuclei over the course of the time lapse using the Stackreg plugin for ImageJ (Thevenaz *et al.*, 1998). Intensity normalization was performed using easyFRAP software (Rapsomaniki *et al.*, 2012). This normalization is designed to adjust for background signal, differences in starting intensity of the photobleached region, and differences in the total fluorescence over the course of the time lapse. The software first subtracts the background intensity from the intensity of the nucleus and the photobleached region at every time point, and then calculates the average fluorescence intensity of the nucleus and the average fluorescence intensity of the photobleached region before photobleaching. The normalization is then calculated at each time point (t) with the following equation: $F(t) = \frac{N_{pre}}{N(t)} * \frac{B(t)}{B_{pre}}$ where $F(t)$ is the normalized fluorescence at each time point, N_{pre} is the average intensity of the nucleus before the photobleach, $N(t)$ is the intensity of the nucleus at each time point, $B(t)$ is the average intensity of the bleached region at each time point, and B_{pre} is the average intensity of the bleached region before the photobleach (Rapsomaniki *et al.*, 2012).

Given the relatively linear nature of the fluorescence recovery and the technical difficulties associated with performing a time lapse long enough for complete recovery, we utilized the following methods to quantify dynamics. The recovery rate was defined as the slope of the normalized postbleach values calculated using the least squares method for each nucleus. Outliers that fell outside of the 1.5 interquartile range were removed. To calculate the amount of recovery over 60 min ($MF_{0–60\ min}$) from average curves, the easyFRAP normalized data were first averaged at each time point for all nuclei from a given condition. Based on these average normalized data, the value immediately after photobleaching was subtracted from the maximum value reached during the 60-min postbleach time interval. This analysis produced the data labeled "60 min recovery by average curve." To calculate $MF_{0–60\ min}$ using data from individual nuclei, we utilized the nonnormalized mean intensity values measured within the photobleached region, calculating individual $MF_{0–60\ min}$ values as follows: $MF_{0–60\ min} = (I_{max}–I_{post})/(I_{pre}–I_{post})$, where I_{max} = maximum intensity value reached during the 60-min postbleach time interval, I_{post} = intensity value immediately after photobleaching, and I_{pre} = intensity value before photobleaching. These $MF_{0–60\ min}$ values were then averaged for a given condition to produce the data labeled "60 min recovery for individual nuclei."

To determine cell cycle state after performing FRAP time lapses, cells were washed three times with PBS, stained with Hoechst 33342 stain (Sigma; 14533) at a concentration of 20 µg/ml in PBS for 5 min, and then washed three times with PBS. Nuclei were imaged via confocal microscopy, and z-stacks were acquired with a 0.2-µm step size. Maximum Hoechst staining intensity values were plotted as a histogram and regions were assigned as G1, S, or G2 based on the shape of the histogram as previously described (see Supplemental Figure S4A; Roukos *et al.*, 2015).

Transfections

Transfections were carried out using lipofectamine 3000 following the manufacturer's instructions for combined DNA/siRNA transfection with the minimum amount of lipofectamine (ThermoFisher; L3000015). In addition to the indicated siRNAs, cells were cotransfected with a pEmCherry-C2 plasmid (a modified version of pEGFP-C2 provided by Anne Schlaitz, Heidelberg University) to identify transfected cells. Cells were transfected in 35-mm dishes with 1.25 µg DNA and 15 pmol siRNA. Transfections were performed twice at 24-h intervals, then assays were carried out 48 h later. For FRAP experiments, transfections were performed in µ-Slide 2 Well dishes (Ibidi; 80286) the same way, except using 0.55 µg DNA and 6.5 pmol siRNA. We used immunofluorescence rather than Western blots to confirm knockdowns because protein levels in individual cells can be measured by immunofluorescence.

ACKNOWLEDGMENTS

We thank Karen White (University of Wyoming) for her assistance with cell culture. This work was supported by the National Institutes of Health/National Institute of General Medical Sciences (Grants no. R35GM134885 and no. P20GM103432).

REFERENCES

Ang SL, Wierda A, Wong D, Stevens KA, Cascio S, Rossant J, Zaret KS (1993). The formation and maintenance of the definitive endoderm lineage in the mouse: involvement of HNF3/forkhead proteins. Development 119, 1301–1315.

Beby F, Lamonerie T (2013). The homeobox gene Otx2 in development and disease. Exp Eye Res 111, 9–16.

Belmont AS, Zhai Y, Thilenius A (1993). Lamin B distribution and association with peripheral chromatin revealed by optical sectioning and electron microscopy tomography. J Cell Biol 123, 1671–1685.

Beppu H, Kawabata M, Hamamoto T, Chytil A, Minowa O, Noda T, Miyazono K (2000). BMP type II receptor is required for gastrulation and early development of mouse embryos. Dev Biol 221, 249–258.
Berezney R, Coffey DS (1974). Identification of a nuclear protein matrix. Biochem Biophys Res Commun 60, 1410–1417.
Berk JM, Tifft KE, Wilson KL (2013). The nuclear envelope LEM-domain protein emerin. Nucleus 4, 298–314.
Broers JL, Machiels BM, Kuijpers HJ, Smedts F, van den Kieboom R, Raymond Y, Ramaekers FC (1997). A- and B-type lamins are differentially expressed in normal human tissues. Histochem Cell Biol 107, 505–517.
Clever M, Funakoshi T, Mimura Y, Takagi M, Imamoto N (2012). The nucleoporin ELYS/Mel28 regulates nuclear envelope subdomain formation in HeLa cells. Nucleus 3, 187–199.
Conlon FL, Lyons KM, Takaesu N, Barth KS, Kispert A, Herrmann B, Robertson EJ (1994). A primary requirement for nodal in the formation and maintenance of the primitive streak in the mouse. Development 120, 1919–1928.
Constantinescu D, Gray HL, Sammak PJ, Schatten GP, Csoka AB (2006). Lamin A/C expression is a marker of mouse and human embryonic stem cell differentiation. Stem Cells 24, 177–185.
Cristofoli F, Moss T, Moore HW, Devriendt K, Flanagan-Steet H, May M, Jones J, Roelens F, Fons C, Fernandez A, *et al.* (2020). De novo variants in LMNB1 cause pronounced syndromic microcephaly and disruption of nuclear envelope integrity. Am J Hum Genet 107, 753–762.
Dahl KN, Scaffidi P, Islam MF, Yodh AG, Wilson KL, Misteli T (2006). Distinct structural and mechanical properties of the nuclear lamina in Hutchinson-Gilford progeria syndrome. Proc Natl Acad Sci USA 103, 10271–10276.
Davis S, Miura S, Hill C, Mishina Y, Klingensmith J (2004). BMP receptor IA is required in the mammalian embryo for endodermal morphogenesis and ectodermal patterning. Dev Biol 270, 47–63.
De Castro SC, Malhas A, Leung KY, Gustavsson P, Vaux DJ, Copp AJ, Greene ND (2012). Lamin B1 polymorphism influences morphology of the nuclear envelope, cell cycle progression, and risk of neural tube defects in mice. PLoS Genet 8, e1003059.
Dobrzynska A, Gonzalo S, Shanahan C, Askjaer P (2016). The nuclear lamina in health and disease. Nucleus 7, 233–248.
Dwyer N, Blobel G (1976). A modified procedure for the isolation of a pore complex-lamina fraction from rat liver nuclei. J Cell Biol 70, 581–591.
Edens LJ, Dilsaver MR, Levy DL (2017). PKC-mediated phosphorylation of nuclear lamins at a single serine residue regulates interphase nuclear size in *Xenopus* and mammalian cells. Mol Biol Cell 28, 1389–1399.
Ellenberg J, Siggia ED, Moreira JE, Smith CL, Presley JF, Worman HJ, Lippincott-Schwartz J (1997). Nuclear membrane dynamics and reassembly in living cells: targeting of an inner nuclear membrane protein in interphase and mitosis. J Cell Biol 138, 1193–1206.
Fiserova J, Maninova M, Sieger T, Uhlirova J, Sebestova L, Efenberkova M, Capek M, Fiser K, Hozak P (2019). Nuclear pore protein TPR associates with lamin B1 and affects nuclear lamina organization and nuclear pore distribution. Cell Mol Life Sci 76, 2199–2216.
Gerace L, Blobel G (1980). The nuclear envelope lamina is reversibly depolymerized during mitosis. Cell 19, 277–287.
Guelen L, Pagie L, Brasset E, Meuleman W, Faza MB, Talhout W, Eussen BH, de Klein A, Wessels L, de Laat W, van Steensel B (2008). Domain organization of human chromosomes revealed by mapping of nuclear lamina interactions. Nature 453, 948–951.
Hoffmann K, Dreger CK, Olins AL, Olins DE, Shultz LD, Lucke B, Karl H, Kaps R, Muller D, Vaya A, *et al.* (2002). Mutations in the gene encoding the lamin B receptor produce an altered nuclear morphology in granulocytes (Pelger-Huet anomaly). Nat Genet 31, 410–414.
Jacob A, Budhiraja S, Reichel RR (1997). Differential induction of HNF-3 transcription factors during neuronal differentiation. Exp Cell Res 234, 277–284.
Kittisopikul M, Shimi T, Tatli M, Tran JR, Zheng Y, Medalia O, Jaqaman K, Adam SA, Goldman RD (2021). Computational analyses reveal spatial relationships between nuclear pore complexes and specific lamins. J Cell Biol 220, e202007082.
Kochin V, Shimi T, Torvaldson E, Adam SA, Goldman A, Pack CG, Melo-Cardenas J, Imanishi SY, Goldman RD, Eriksson JE (2014). Interphase phosphorylation of lamin A. J Cell Sci 127, 2683–2696.
Lin F, Worman HJ (1993). Structural organization of the human gene encoding nuclear lamin A and nuclear lamin C. J Biol Chem 268, 16321–16326.
Lukášová E, Kova ik A, Ba ikova A, Falk M, Kozubek S (2017). Loss of lamin B receptor is necessary to induce cellular senescence. Biochem J 474, 281–300.
Meuleman W, Peric-Hupkes D, Kind J, Beaudry JB, Pagie L, Kellis M, Reinders M, Wessels L, van Steensel B (2013). Constitutive nuclear lamina-genome interactions are highly conserved and associated with A/T-rich sequence. Genome Res 23, 270–280.
Mishina Y, Suzuki A, Ueno N, Behringer RR (1995). Bmpr encodes a type I bone morphogenetic protein receptor that is essential for gastrulation during mouse embryogenesis. Genes Dev 9, 3027–3037.
Moir RD, Yoon M, Khuon S, Goldman RD (2000). Nuclear lamins A and B1: different pathways of assembly during nuclear envelope formation in living cells. J Cell Biol 151, 1155–1168.
Nichols J, Zevnik B, Anastassiadis K, Niwa H, Klewe-Nebenius D, Chambers I, Scholer H, Smith A (1998). Formation of pluripotent stem cells in the mammalian embryo depends on the POU transcription factor Oct4. Cell 95, 379–391.
Nikolakaki E, Mylonis I, Giannakouros T (2017). Lamin B receptor: interplay between structure, function and localization. Cells 6, 28.
Olins AL, Rhodes G, Welch DB, Zwerger M, Olins DE (2010). Lamin B receptor: multi-tasking at the nuclear envelope. Nucleus 1, 53–70.
Padiath QS, Saigoh K, Schiffmann R, Asahara H, Yamada T, Koeppen A, Hogan K, Ptacek LJ, Fu YH (2006). Lamin B1 duplications cause autosomal dominant leukodystrophy. Nat Genet 38, 1114–1123.
Parry DA, Martin CA, Greene P, Marsh JA, Genomics England Research Consortium, Blyth M, Cox H, Donnelly D, Greenhalgh L, Greville-Heygate S, *et al.* (2021). Heterozygous lamin B1 and lamin B2 variants cause primary microcephaly and define a novel laminopathy. Genet Med 23, 408–414.
Pascual-Reguant L, Blanco E, Galan S, Le Dily F, Cuartero Y, Serra-Bardenys G, Di Carlo V, Iturbide A, Cebria-Costa JP, Nonell L, *et al.* (2018). Lamin B1 mapping reveals the existence of dynamic and functional euchromatin lamin B1 domains. Nat Commun 9, 3420.
Peric-Hupkes D, Meuleman W, Pagie L, Bruggeman SW, Solovei I, Brugman W, Graf S, Flicek P, Kerkhoven RM, van Lohuizen M, *et al.* (2010). Molecular maps of the reorganization of genome-nuclear lamina interactions during differentiation. Mol Cell 38, 603–613.
Peter M, Kitten GT, Lehner CF, Vorburger K, Bailer SM, Maridor G, Nigg EA (1989). Cloning and sequencing of cDNA clones encoding chicken lamins A and B1 and comparison of the primary structures of vertebrate A- and B-type lamins. J Mol Biol 208, 393–404.
Rapsomaniki MA, Kotsantis P, Symeonidou IE, Giakoumakis NN, Taraviras S, Lygerou Z (2012). easyFRAP: an interactive, easy-to-use tool for qualitative and quantitative analysis of FRAP data. Bioinformatics 28, 1800–1801.
Reddy KL, Zullo JM, Bertolino E, Singh H (2008). Transcriptional repression mediated by repositioning of genes to the nuclear lamina. Nature 452, 243–247.
Rober RA, Weber K, Osborn M (1989). Differential timing of nuclear lamin A/C expression in the various organs of the mouse embryo and the young animal: a developmental study. Development 105, 365–378.
Roberts B, Haupt A, Tucker A, Grancharova T, Arakaki J, Fuqua MA, Nelson A, Hookway C, Ludmann SA, Mueller IA, *et al.* (2017). Systematic gene tagging using CRISPR/Cas9 in human stem cells to illuminate cell organization. Mol Biol Cell 28, 2854–2874.
Roukos V, Pegoraro G, Voss TC, Misteli T (2015). Cell cycle staging of individual cells by fluorescence microscopy. Nat Protoc 10, 334–348.
Roux KJ, Kim DI, Raida M, Burke B (2012). A promiscuous biotin ligase fusion protein identifies proximal and interacting proteins in mammalian cells. J Cell Biol 196, 801–810.
Saunders A, Faiola F, Wang J (2013). Concise review: pursuing self-renewal and pluripotency with the stem cell factor Nanog. Stem Cells 31, 1227–1236.
Schindelin J, Arganda-Carreras I, Frise E, Kaynig V, Longair M, Pietzsch T, Preibisch S, Rueden C, Saalfeld S, Schmid B, *et al.* (2012) Fiji: an open-source platform for biological-image analysis. Nat Methods 9, 676–682.
Shimi T, Pfleghaar K, Kojima S, Pack CG, Solovei I, Goldman AE, Adam SA, Shumaker DK, Kinjo M, Cremer T, Goldman RD (2008). The A- and B-type nuclear lamin networks: microdomains involved in chromatin organization and transcription. Genes Dev 22, 3409–3421.
Smith J (1997). Brachyury and the T-box genes. Curr Opin Genet Dev 7, 474–480.
Solovei I, Wang AS, Thanisch K, Schmidt CS, Krebs S, Zwerger M, Cohen TV, Devys D, Foisner R, Peichl L, *et al.* (2013). LBR and lamin A/C sequentially tether peripheral heterochromatin and inversely regulate differentiation. Cell 152, 584–598.
Takeshi S, Pack CG, Goldman RD (2016). Analyses of the dynamic properties of nuclear lamins by fluorescence recovery after photobleaching (FRAP) and fluorescence correlation spectroscopy (FCS). Methods Mol Biol 1411, 99–111.

Thevenaz P, Ruttimann UE, Unser M (1998). A pyramid approach to subpixel registration based on intensity. IEEE Trans Image Process 7, 27–41.
Turgay Y, Eibauer M, Goldman AE, Shimi T, Khayat M, Ben-Harush K, Dubrovsky-Gaupp A, Sapra KT, Goldman RD, Medalia O (2017). The molecular architecture of lamins in somatic cells. Nature 543, 261–264.
van Steensel B, Henikoff S (2000). Identification of in vivo DNA targets of chromatin proteins using tethered Dam methyltransferase. Nat Biotechnol 18, 424–428.
Vergnes L, Peterfy M, Bergo MO, Young SG, Reue K (2004). Lamin B1 is required for mouse development and nuclear integrity. Proc Natl Acad Sci USA 101, 10428–10433.
Vogel MJ, Peric-Hupkes D, van Steensel B (2007). Detection of in vivo protein-DNA interactions using DamID in mammalian cells. Nat Protoc 2, 1467–1478.
Vorburger K, Lehner CF, Kitten GT, Eppenberger HM, Nigg EA (1989). A second higher vertebrate B-type lamin. cDNA sequence determination and in vitro processing of chicken lamin B2. J Mol Biol 208, 405–415.
Waterham HR, Koster J, Mooyer P, Noort Gv G, Kelley RI, Wilcox WR, Wanders RJ, Hennekam RC, Oosterwijk JC (2003). Autosomal recessive HEM/Greenberg skeletal dysplasia is caused by 3 beta-hydroxysterol delta 14-reductase deficiency due to mutations in the lamin B receptor gene. Am J Hum Genet 72, 1013–1017.
Winnier G, Blessing M, Labosky PA, Hogan BL (1995). Bone morphogenetic protein-4 is required for mesoderm formation and patterning in the mouse. Genes Dev 9, 2105–2116.
Wong X, Cutler JA, Hoskins VE, Gordon M, Madugundu AK, Pandey A, Reddy KL (2021). Mapping the micro-proteome of the nuclear lamina and lamina-associated domains. Life Sci Alliance 4, e202000774.
Worman HJ, Bonne G (2007). "Laminopathies": a wide spectrum of human diseases. Exp Cell Res 313, 2121–2133.
Zhironkina OA, Kurchashova SY, Pozharskaia VA, Cherepanynets VD, Strelkova OS, Hozak P, Kireev II (2016). Mechanisms of nuclear lamina growth in interphase. Histochem Cell Biol 145, 419–432.
Zuleger N, Kelly DA, Richardson AC, Kerr AR, Goldberg MW, Goryachev AB, Schirmer EC (2011). System analysis shows distinct mechanisms and common principles of nuclear envelope protein dynamics. J Cell Biol 193, 109–123.
Zuo B, Yang J, Wang F, Wang L, Yin Y, Dan J, Liu N, Liu L (2012). Influences of lamin A levels on induction of pluripotent stem cells. Biol Open 1, 1118–1127.